# Effect of hybridization of continuous and discontinuous tape composites on stiffness and strength

## A computational analysis

Gulmez, Deniz Ezgi; Turteltaub, Sergio

**DOI**
10.1016/j.compstruct.2025.119313

**Publication date**
2025

**Document Version**
Final published version

**Published in**
Composite Structures

Composite Structures 370 (2025) 119313

Contents lists available at ScienceDirect

Composite Structures

journal homepage: www.elsevier.com/locate/compstruct

# Effect of hybridization of continuous and discontinuous tape composites on stiffness and strength: A computational analysis

Deniz Ezgi Gulmez *, Sergio Turteltaub

*Department of Aerospace Structures & Materials, Faculty of Aerospace Engineering, Delft University of Technology, Kluyverweg 1, Delft 2629 HS, The Netherlands*

ARTICLE INFO

*Keywords:*
Continuous–discontinuous tape composites
Hybrid CFRP
Effective flexural strength
Effective tensile strength

ABSTRACT

Numerical investigations were conducted to explore the mechanical response of hybrid layered continuous–discontinuous tape composites focusing on damage initiation and ultimate strength under both tensile and bending loads. These composites combine layers of continuous unidirectional tapes with layers of randomly oriented short (discontinuous) tapes. A series of laminated specimens was analyzed, representing various strategies to create hybrid combinations as well as the limit cases of pure continuous and pure discontinuous tapes. The hybrid architectures consist of different stacking sequences and varying ratios of continuous and discontinuous plies. Detailed mesoscale simulations were performed utilizing a finite element model that explicitly incorporates the ply-level arrangements of both continuous and discontinuous plies. By means of numerical homogenization, the effective elastic stiffness and strength of each configuration were determined, enabling the establishment of scaling laws for these properties with respect to spatial variability and the ratio of continuous to discontinuous tape content. These findings serve as a roadmap for optimizing the blend of these two types of tape to meet specific mechanical performance targets, thereby advancing the development of more sustainable and high-performing composites.

## 1. Introduction

Lightweight and durable structures are crucial in aerospace, automotive, and wind energy industries, driving the increased use of carbon- and glass-fiber-reinforced composites due to their high stiffness-to-mass density ratio. Despite their excellent mechanical properties, these materials face challenges such as limited fracture energy, resulting in brittle failures, and environmental concerns related to waste generation. To address these issues, researchers are developing innovative zero waste processes, recyclable materials, and reuse techniques to minimize environmental impact and improve material toughness [1–6].

Discontinuous Tape (DT) thermoplastic composites, also known as chopped tape thermoplastic composites, enhance toughness and prevent catastrophic failure, though at the cost of reduced elastic stiffness and fracture strength compared to Continuous Tape (CT) composites. DT composites, made from short tapes layered in random or biased orientations, achieve pseudoductility through interfacial slip, allowing progressive failure and improved damage tolerance [7,8]. Pimenta and Robinson [9] improved an analytical shear-lag model to show the influence of highly aligned discontinuities on mechanical performance. Czél et al. [10] validated this influence experimentally, providing a prior warning before failure. Johanson et al. [11] utilized Digital Image Correlation (DIC) to investigate the initiation of damage in DT composites based on the local strain field, revealing the progression of failure. Similarly to the activating effect of pseudoductility observed with fiber reorientation [12,13] and hybridization methods [14–16], these approaches lead to controlled failure modes and enhanced toughness, rendering composites more resilient to various loading conditions and reducing the likelihood of catastrophic failures.

While DT composites exhibit good pseudoductility, their significant spatial variability, discontinuity, and complexity result in lower elastic stiffness and fracture strength [17–22]. To address these challenges, researchers are exploring innovative solutions to enhance DT composite performance. One promising approach is the *hybridization* of continuous and discontinuous tapes, which enables ductile failure while maintaining relatively high stiffness and strength. Furthermore, the concept of hybrid continuous–discontinuous tape composites can be extended to include systems with layers of recycled excess material (e.g., nesting surplus and trimmings), instead of pristine prepreg platelets, which would reduce waste in a closed-loop manufacturing cycle [23].

Trauth and Weidenmann [24] investigated the effect of hybridization on mechanical properties by combining continuous carbon fiber

* Corresponding author.
*E-mail address:* D.E.Gulmez@tudelft.nl (D.E. Gulmez).

https://doi.org/10.1016/j.compstruct.2025.119313
Received 13 December 2024; Received in revised form 13 May 2025; Accepted 21 May 2025
Available online 5 June 2025

and discontinuous glass fiber. They observed a significant increase in tensile and compressive modulus of elasticity in fiber direction. Additionally, they noted increased puncture energy and maximum force under quasi-static puncture tests [25]. Hasan et al. [26] reinforced discontinuous carbon fiber with continuous glass filaments to improve the impact strength of the composites. Hybridization plays a key role in determining composite performance under various conditions, making further research essential to refine predictive models and ensure reliable industrial applications [27,28]. As an example of architectural hybridization of discontinuous tape composites, Visweswaraiah et al. [29,30] integrated discontinuous with continuous laminate groups. Combining different fiber architectures in specific stacking configurations significantly enhances mechanical properties such as tensile strength and stiffness while reducing warpage and strand waviness. Synergetic effects result in hybrid configurations outperforming individual components by up to 25%, with superior interlaminar shear strength due to improved load sharing. A semi-empirical model effectively predicts these behaviors and synergies, potentially streamlining the testing process.

The concept of hybrid continuous–discontinuous thermoplastic composites addresses two key issues: (i) creating a lightweight material with a balance between stiffness and damage tolerance, and (ii) incorporating recycled excess material for a zero-waste manufacturing cycle. Continuous tapes enhance stiffness, while discontinuous tapes improve damage tolerance. A critical aspect is how to combine these tapes to achieve the desired mechanical properties in the hybrid material.

This work develops a computational framework to analyze the effect of the spatial architecture of continuous and discontinuous tapes on the elastic stiffness and strength of hybrid materials under various loading conditions. By integrating hybrid configurations, challenges such as stair-step surfaces and singularities in discontinuous tape layers are addressed, providing a more accurate mesoscale mechanical response. The approach enables detailed analysis of damage initiation in hybrid laminate coupons, with a novel focus on determining fracture strength under flexural loading, which is critical for thin-walled structures.

The flexural behavior of discontinuous fiber-reinforced composites has been investigated to understand damage mechanisms and improve predictive capabilities. Nakashima et al. [31] developed an analytical model for ultra-thin chopped carbon fiber tape-reinforced thermoplastics (UT-CTT), showing the influence of fiber orientation and tape geometry on flexural properties. However, their model did not address progressive damage mechanisms. Tang et al. [32] explored bending fatigue in chopped carbon fiber composites using a hybrid micro-macro model, which accurately captured fatigue life but was computationally demanding for large-scale simulations. Similarly, Qu et al. [33] used a peridynamics-based model to analyze the flexural response of composites, demonstrating the method's capability in handling discontinuities. While peridynamics has been widely applied in solid mechanics for fracture analysis and damage modeling (e.g., Zhang et al. [34]), its application in stress concentration analysis and specific damage modes in hybrid composites remains limited.

The present study adopts the Hashin failure criteria-based FEM model to predict both the flexural and tensile response of composites for modeling intralaminar damage mechanisms, such as matrix cracking and fiber breakage, achieving a balance between accuracy and computational feasibility. Various configurations are analyzed, generating scaling relations to determine optimal spatial arrangements and tape proportions for achieving target hybrid material properties. This approach helps identify the best balance between mechanical efficiency and hybridization ratio, contributing to more resilient, sustainable structures in aerospace, automotive, and wind energy applications while minimizing waste.

The article is structured as follows: Section 2 outlines the hybrid configurations and simulation methodology. Section 4 presents results for selected configurations under tension and bending loading. Section 5 conducts a parametric analysis to explore the dependence of elastic properties on configuration characteristics, including spatial arrangement and continuous tape volume. Section 6 focuses on detectable initial and ultimate strength. The final section offers concluding remarks and future work recommendations.

## 2. Hybrid configurations and simulation methodology

### 2.1. Generation of CT-DT hybrid configurations

To study the effect of continuous tape content and its spatial distribution in hybrid materials, numerical coupon-like samples are generated by combining layers of unidirectional continuous tapes and randomly-oriented discontinuous tapes. While both tapes share the same material, their effective properties differ in stiffness and strength, treating them as distinct materials. The primary variable characterizing the hybrid material is the ratio of continuous to discontinuous tapes, referred to as the *hybridization ratio*. Three layered configurations are considered in the present study, namely (i) *inward-to-outward* placement of CT layers (Fig. 1(a) and labeled as S1C*n*), (ii) *outward-to-inward* placement of CT layers (Fig. 1(b), and labeled as S2C*n*), and (iii) *intercalated* placement sequences of DT and CT layers (Fig. 1 (c), and labeled as S3C*n*). These configurations are selected for their compatibility with existing manufacturing techniques and relevance to thin-walled structures. Details on generating random DT layers are provided in [35].

The laminated samples for all configurations consist of $N = 20$ layers, with each layer having the same volume. The number of layers is chosen based on convergence studies for the average mechanical properties of a laminate [35]. For inward-to-outward and outward-to-inward configurations, hybridization ratios were varied in 10% increments from 0% (all discontinuous tapes) to 100% (all continuous tapes). Intercalated samples were generated with hybridization ratios of 25%, 50% and 75%, along with several sub-configurations labeled as S3C*n* (Fig. 1). The samples are arranged in anticipation of possible effects in the case of bending since failure under tension differs from failure under compression and the outer layers are more relevant than the inner layers.

For a 50% hybridization ratio, sample S3C1 features a fine layer-by-layer intercalation. S3C2 and S3C3 are intercalated every two layers, with a shift between them. S3C5 uses a coarser intercalation (every three layers), while S3C6, similar to S3C5, includes an extra continuous tape layer, resulting in a 55% hybridization ratio. Notably, S3C6 has continuous tapes on both the top and bottom layers.

At higher hybridization ratios (i.e., 75% continuous tapes), two shifted variants, S3C7 and S3C8, are analyzed, while a single sample, S3C9, represents the lower ratio (25%). In the 25% configuration, continuous tape layers are placed away from the top and bottom. While not covering all possible arrangements, these configurations capture the key features needed to explore the hybrid material design space.

A typical computational sample in Fig. 2 includes (a) individual layers of randomly oriented tapes, (b) layer-wise volume-filling orientations, (c) integrated coupon-like specimen and (d) a detailed through-the-thickness magnified view. The samples, similar in dimensions to those in [35], exclude a 10 mm border to mitigate edge alignment effects in DT layers, ensuring an unbiased random distribution. The final dimensions are 150 mm × 40 mm × 2 mm.

In the finite element modeling, all layers are explicitly represented with their local fiber orientations, without through-the-thickness averaging. A mesoscale modeling approach is adopted, where the microscale is captured through effective constitutive tape properties, the mesoscale is explicitly modeled with layer-wise configurations, and the macroscale laminate behavior is obtained via numerical homogenization of mesoscale simulation results under various loading conditions.

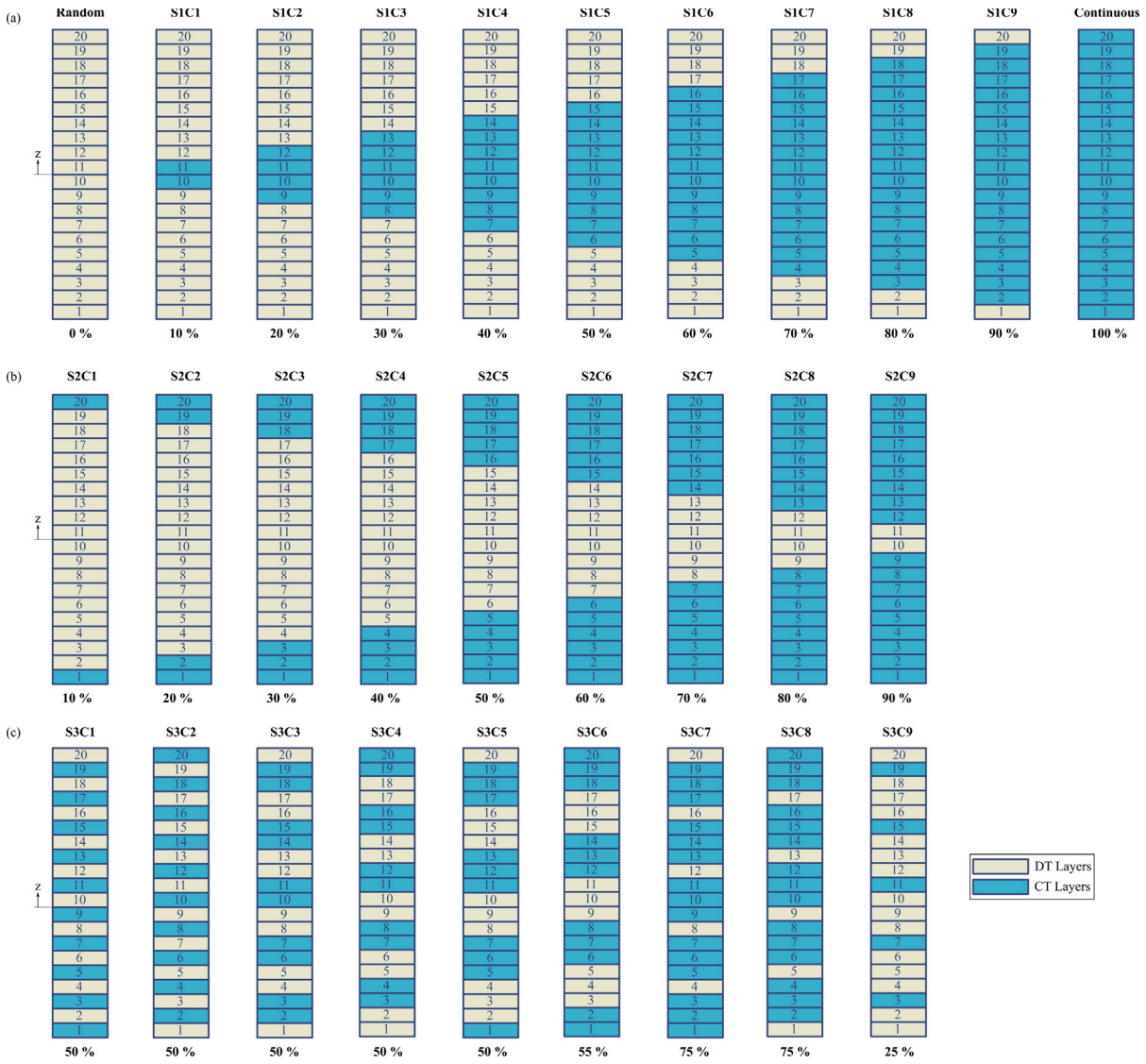


**Fig. 1.** Configurations of specimens based on continuous tapes (a) inward-to-outward, labeled as S1C*n*, (b) outward-to-inward, labeled as S2C*n*, (c) intercalated placements, labeled as S3C*n*.

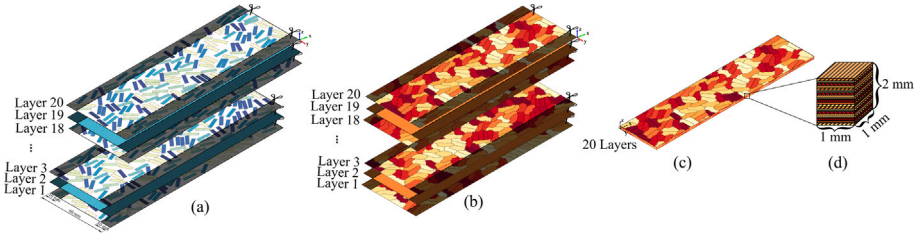


**Fig. 2.** Schematic representation of (a) virtual layers of non-overlapping continuous and discontinuous tapes, (b) ply-wise volume-filling tapes (c) assembled CT-DT hybrid laminate (d) detailed through-the-thickness laminated structure.

### 2.2. Numerical implementation

The hybrid CT-DT specimens described in Section 2.1 are meshed using 8-noded continuum shell elements (Abaqus SC8R) with dimensions 1 mm × 1 mm × 0.1 mm (one element per layer). A mesh convergence analysis with $3 \cdot 10^4$, $1.2 \cdot 10^5$ and $4.8 \cdot 10^5$ elements showed a peak load error of less than 2%. Each element is assigned a local fiber orientation and corresponding material properties based on the configuration.

Due to the heterogeneous nature of the specimens, applying uniform point-wise kinematic boundary conditions does not accurately reflect actual conditions, especially under bending. To address this, 8-noded brick elements (Abaqus C3D8R) were added as tabs at the specimen ends, as shown in Fig. 3. These tabs allow uniform boundary conditions to transition into non-uniform conditions at the interface, transmitting the applied force and displacement while preventing premature failure due to overly-stiff boundary conditions in heterogeneous systems.

All analyses were executed under quasi-static loading conditions and solved using implicit time integration (Abaqus Standard FEM

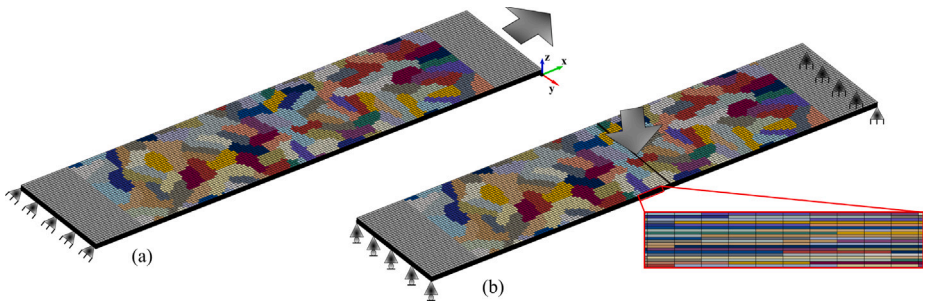


**Fig. 3.** Boundary conditions of specimens under (a) Tensile and (b) Bending load.

**Table 1**
Elastic properties of CF/PEEK [19] and AS4/PPS composite with a fiber volume ratio of 59% [36].

| Property | CF/PEEK | AS4/PPS | Units |
|---|---|---|---|
| Longitudinal Young's modulus, $E_f$ | 130 | 128 | GPa |
| Transverse Young's modulus, $E_m$ | 10 | 10.1 | GPa |
| Shear modulus, $G_{fm}$ | 5.2 | 5.7 | GPa |
| Longitudinal Poisson's ratio, $\nu_{fm}$ | 0.33 | 0.37 | – |

package). Boundary conditions in tensile analyses were defined under simply-supported conditions in combination with a uniform displacement applied point-wise on one face at a quasi-static rate in the $x$-direction (Fig. 3(a)). For bending analyses, the displacement of the lower edge on the left side of specimen was constrained (zero displacement in all directions) while the lower edge of the right side was specified in accordance with a roller support (restriction only in the $z$-direction). The mid-section of the specimen is subsequently displaced downwards to mimic the conditions encountered in a three-point bending test as shown in Fig. 3(b).

### 2.3. Mechanical models and material properties

The continuous and discontinuous tapes are assumed to be made of the same material system. Two systems are considered in the present study, namely CF/PEEK (carbon fiber/polyether ether ketone) and AS4/PPS (carbon fiber/polyphenylene sulphide) unidirectional (UD) prepregs. The first system is used in conjunction with experimental results of laminates with discontinuous tapes for validation of the numerical model. The hybrid material design analysis is carried out with the second system. PPS-based systems have slightly lower properties than PEEK-based systems but they have relatively lower costs. The elastic properties of CF/PEEK and AS4/PPS are indicated in Table 1, including the Young's moduli $E_f$ and $E_m$, with the index f representing the local fiber direction (longitudinal) and m the transverse direction, which is dominated by the response of the matrix material, the shear modulus $G_{fm}$ and the Poisson's ratio $\nu_{fm}$.

Damage initiation in the composite material is detected based on Hashin's failure criteria [37] including four damage mechanisms, namely (i) fiber tension, (ii) fiber compression, (iii) matrix tension, and (iv) matrix compression. The aforementioned damage mechanisms are characterized by material parameters $\sigma_f^t$, $\sigma_f^c$, $\sigma_m^t$, $\sigma_m^c$, $\tau^l$, $\tau^t$ that refer to, respectively, the fracture strength $\sigma_f$ in the longitudinal fiber direction under tension (t) and compression (c), the fracture strength $\sigma_m$ in the transverse fiber direction under tension (t) and compression (c) and the shear strengths $\tau$ in the longitudinal (l) and transverse (s) directions.

When the damage initiation criterion of one of the four failure mechanisms is satisfied, further loading induces the degradation of material stiffness coefficients, as described by the in-plane damaged stiffness matrix $\boldsymbol{C}_d$ such that the in-plane stress response of the damaged material is given as

$$\boldsymbol{\sigma} = \boldsymbol{C}_d \boldsymbol{\epsilon} \tag{1}$$

where

$$\boldsymbol{\sigma} = \begin{bmatrix} \sigma_{11} \\ \sigma_{22} \\ \tau_{12} \end{bmatrix} \qquad \boldsymbol{\epsilon} = \begin{bmatrix} \epsilon_{11} \\ \epsilon_{22} \\ \gamma_{12} \end{bmatrix}$$

are the in-plane components of the stress and strain tensors with $\gamma_{12} = 2\epsilon_{12}$.

The reduction in stiffness coefficients is modulated by damage variables, which can assume values ranging from zero (indicating an undamaged state) to one (representing a fully damaged state for the mode corresponding to that particular damage variable). The evolution of damage is modeled based on the various fracture mechanisms, with limit values $G_f$ in the fiber direction and $G_m$ in the transverse direction, which are dominated by the fiber and matrix fracture properties respectively. It is assumed that the critical values in tension and compression are the same, i.e., $G_f^t = G_f^c$ and $G_m^t = G_m^c$. The damage variables evolve according to a linear softening relation between an equivalent strain-like variable and an equivalent stress such that complete damage per unit area is achieved when the energy dissipated is equal to the critical value. Fracture energy values for the system analyzed in the present work, made of UD tapes of CF/PEEK or AS4/PPS tapes are indicated in Table 2.

To enhance convergence and mitigate numerical difficulties, a viscous regularization was employed, with numerical viscosity $7.5 \cdot 10^{-4}$ s, chosen as the smallest value that provides a convergent result.

### 2.4. Sample homogenization

A homogenization scheme similar to Classical Laminated Plate Theory was implemented to provide insight into the effective mechanical response of hybrid continuous–discontinuous tape composites under various loading conditions. The in-plane forces per unit width, referred to as force resultants and denoted as $N_{11}$, $N_{22}$, and $N_{12}$, are computed as

$$N_{\alpha\beta} = \int_{-t/2}^{t/2} \sigma_{\alpha\beta} \mathrm{d}x_3 = \sum_{k=1}^{N} \int_{z_{k-1}}^{z_k} \sigma_{\alpha\beta} \mathrm{d}x_3 \qquad \alpha, \beta = 1, 2 \,, \tag{2}$$

where the through-the-thickness integration is carried out in the domain shown in Fig. 3(c), with $t$ representing the thickness and $z_k$ indicating the $x_3$-coordinate of the $k$th layer. Similarly, the moments per unit width, referred to as moment resultants and denoted as $M_{11}$, $M_{22}$, and $M_{12}$, are computed as

$$M_{\alpha\beta} = \int_{-t/2}^{t/2} \sigma_{\alpha\beta} x_3 \mathrm{d}x_3 = \sum_{k=1}^{N} \int_{z_{k-1}}^{z_k} \sigma_{\alpha\beta} x_3 \mathrm{d}x_3 \qquad \alpha, \beta = 1, 2 \,. \tag{3}$$

After through-the-thickness homogenization, coupon-level effective force resultants (denoted as $\hat{N}_{11}$, $\hat{N}_{22}$, and $\hat{N}_{12}$) and moment resultants (denoted as $\hat{M}_{11}$, $\hat{M}_{22}$, and $\hat{M}_{12}$) are evaluated by integrating the through-the-thickness force and moment resultants over the mid-plane of the coupon (excluding the end tabs) and normalizing the results by dividing by $Lw$, which represents the mid-plane area based on the

**Table 2**
Failure limits and fracture properties of UD CF/PEEK and AS4/PPS composite [19,36,38].

| Property | CF/PEEK | AS4/PPS | Units |
|---|---|---|---|
| Tensile strength in the longitudinal fiber direction, $\sigma_{\mathrm{f}}^{\mathrm{t}}$ | 2280 | 2045 | MPa |
| Compressive strength in the longitudinal fiber direction, $\sigma_{\mathrm{f}}^{\mathrm{c}}$ | 1300 | 1117 | MPa |
| Tensile strength in the transverse fiber direction, $\sigma_{\mathrm{m}}^{\mathrm{t}}$ | 86 | 50 | MPa |
| Compressive strength in the transverse fiber direction, $\sigma_{\mathrm{m}}^{\mathrm{c}}$ | 86 | 90 | MPa |
| In-plane shear strength, $\tau^{\mathrm{l}} = \tau^{\mathrm{s}}$ | 152 | 77 | MPa |
| Fracture Energy in the longitudinal fiber direction, $G_{\mathrm{f}}^{\mathrm{t,c}}$ | 12.5 | 12.5 | kJ/m$^2$ |
| Fracture Energy in the transverse fiber direction, $G_{\mathrm{m}}^{\mathrm{t,c}}$ | 1.0 | 1.0 | kJ/m$^2$ |

length $L$ and width $w$ of the specimen, i.e., the coupon-level effective force resultants are

$$\hat{N}_{\alpha\beta} = \frac{1}{Lw}\int_0^L\int_0^w N_{\alpha\beta}\mathrm{d}x_1\mathrm{d}x_2 \qquad \alpha,\beta = 1,2\ , \tag{4}$$

while the coupon-level effective moment resultants are

$$\hat{M}_{\alpha\beta} = \frac{1}{Lw}\int_0^L\int_0^w M_{\alpha\beta}\mathrm{d}x_1\mathrm{d}x_2 \qquad \alpha,\beta = 1,2\ . \tag{5}$$

The results of all simulations are reported using the coupon-level effective response, with the effective mid-plane strains defined as

$$\hat{\epsilon}_{\alpha\beta} = \frac{1}{Lw}\int_0^L\int_0^w\int_{-t/2}^{t/2}\epsilon_{\alpha\beta}\mathrm{d}x_1\mathrm{d}x_2\mathrm{d}x_3\ , \qquad \alpha,\beta = 1,2\ , \tag{6}$$

and the effective curvatures as

$$\hat{\kappa}_{\alpha\beta} = \frac{1}{Lw}\int_0^L\int_0^w\int_{-t/2}^{t/2}\kappa_{\alpha\beta}\mathrm{d}x_1\mathrm{d}x_2\mathrm{d}x_3 \qquad \alpha,\beta = 1,2\ . \tag{7}$$

The effective laminate response is then expressed as a relation between the in-plane effective force/moment resultants $[\hat{N}_{\alpha\beta}, \hat{M}_{\alpha\beta}]$ and the in-plane effective strain/curvature $[\hat{\epsilon}_{\alpha\beta}, \hat{\kappa}_{\alpha\beta}]$ through the so-called $ABD$-matrix.

### 2.5. Post-processing: criterion for detection of onset of damage

After an initial elastic stage, the hybrid laminate fails at its weakest region(s). As deformation increases, the specimen degrades further, reaching a peak load. Damage then localizes in a narrow region, and the load decreases. The specimen is fully damaged when the load reaches zero. In brittle behavior, the damage onset and peak load are close, while for more damage-tolerant specimens, they are distinctly different.

To characterize the inelastic behavior of hybrid specimens, the onset of failure is identified by the first occurrence of damage in the simulation. However, this approach may underestimate the load for damage initiation, as degradation may be localized and not propagate until the load increases significantly. To standardize damage detection, the criterion is based on the reduction in effective stiffness. For tensile and bending tests, damage onset occurs when the reduction in stiffness, normalized by the initial undamaged stiffness, exceeds a critical threshold. The critical reductions in tensile stiffness ($R_T$) bending stiffness ($R_B$) are given by:

$$R_T = \frac{A_0 - A_{\mathrm{d},0}}{A_0} \tag{8}$$

and

$$R_B = \frac{D_0 - D_{\mathrm{d},0}}{D_0} \tag{9}$$

where $A_0$ and $A_{\mathrm{d},0}$ are the undamaged tensile and bending stiffnesses, respectively, and $D_0$ and $D_{\mathrm{d},0}$ are the damaged stiffnesses at the onset of detectable damage, all measured in the longitudinal direction of the specimens. Based on preliminary parametric analyses monitoring energy dissipation, the following critical values were chosen:

$$R_T = 3,\% \quad R_B = 3\%\ .$$

The progression of damage is a gradual process and there is no precise threshold value. Consequently, the specific threshold value was chosen large enough to prevent a premature detection of damage, while it was small enough to detect a clear change in the dissipation rate (slope as a function of applied strain). These threshold values, though somewhat arbitrary, can be applied systematically and serve as a comparative basis, similar to plasticity thresholds (proof stress) in metals.

## 3. Validation of numerical model for fully-discontinuous specimens

The UD CF/PEEK discontinuous tapes, with dimensions of 22.5 mm × 7.5 mm and a thickness of 0.2 mm, were randomly placed into the mold. The material properties of these tapes are provided in Tables 1 and 2. The mold was positioned in a press, and once the processing temperature of 385 °C was achieved, a full pressure of 35 bar was applied. After maintaining this condition for 15 min, the mold was cooled at an average rate of 10 °C/min. The resulting panel dimensions were 100 mm × 140 mm with a thickness of 4 mm. Three specimens, labeled E1, E2 and E3, were cut from the panel. Each experimental specimen measures 140 mm in length and 25.4 mm in width, with a gauge section of 30 mm × 25.4 mm, constrained by the mold size and the clamps of the tensile testing machine. A tensile load was applied until the specimens ruptured.

The tensile stress versus cross-head displacement curves for the three specimens are shown in Fig. 4. Prior to reaching the ultimate tensile stress, small reductions in stress can be observed in the curves for E1 and E2. This behavior indicates the onset of detectable damage. E3 did not have a clearly identifiable onset of damage.

When tensile loading was applied to the virtual specimens, generated to replicate the size and material of the experimental specimens shown in Fig. 5, damage initiation was identified using a 3% stiffness reduction criterion.

A two-sample t-test was performed to compare the mean scores of the probabilistic virtual and experimental test series. As shown in Fig. 6 the two-sided p-values were 0.4289 for the detectable damage strength data and 0.8045 for the ultimate strength data. Despite the limited number of experimental samples, the results suggest that the predictions for the hybrid structures are realistic and reliable. In particular, the value of 3% stiffness reduction as a criterion for initiation of detectable damage matches the experimental results within a reasonable tolerance. Similarly, the prediction for the ultimate strength is also predicted within a reasonable tolerance. The same approach will be used in subsequent sections for AS4/PPS since the material properties of that system are similar to the ones for CF/PEEK.

## 4. Representative responses under tensile and bending loading

Finite element simulations were carried out with the specimens indicated in Section 2.1 using the boundary conditions indicated in Section 2.2. Correspondingly, the effective mechanical behavior of the hybrid continuous–discontinuous specimens for distinct configurations can be obtained through post-processing and homogenization under tensile and bending loads.

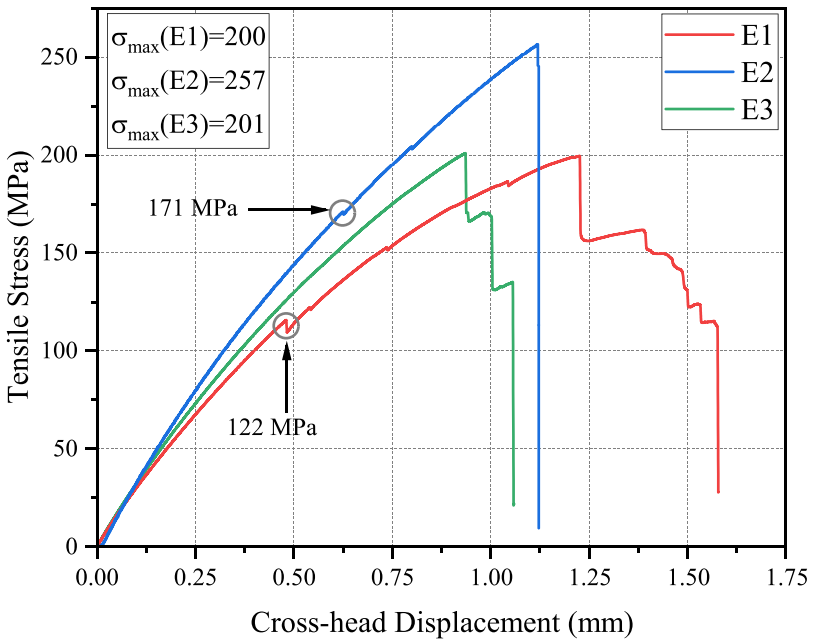


**Fig. 4.** Tensile stress–displacement behavior of experimental specimens.

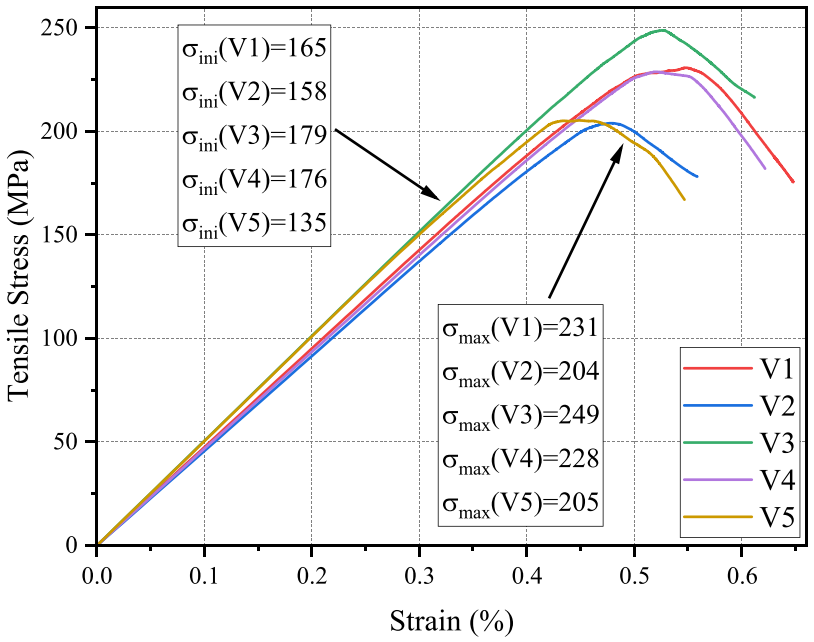


**Fig. 5.** Stress–strain response of virtual specimens under tensile loading. The values for the initial detectable damage $\sigma_{\text{ini}}$ are based on a 3% reduction of the stiffness.

### *4.1. Tensile behavior of distinct configurations*

#### *4.1.1. Fully discontinuous specimen*

The first type of specimens analyzed consists of randomly-oriented discontinuous tapes, expected to exhibit lower elastic stiffness and strength. The specimen is loaded until failure, which in this case is dominated by matrix failure in tension. Fig. 7 depicts the spatial distribution of the matrix failure $d_m$ in tension, where 0 indicates no failure and 1 indicates complete failure. The contour plot is taken at a nominal axial strain of $\hat{\epsilon}_{11} = 0.58\%$, slightly after the ultimate load. Red regions indicate complete matrix failure, typically in short tapes with fibers perpendicular to the load, while blue regions, with fibers aligned in the loading direction, show no matrix failure. Although the figure depicts damage in the top layer, extensive damage occurs throughout all layers. Beyond the ultimate load, damage localizes, and the specimen's ability to carry load significantly degrades, with ultimate failure occurring when the specimen can no longer transmit axial load.

For a fully random sample, the effective axial force resultant $\hat{N}_{11}$ is plotted as a function of the effective axial strain $\hat{\epsilon}_{11}$ in Fig. 8. The response is initially linear until damage is detected, based on the criterion in Section 2.5. The initial detectable damage occurs at an axial strain of 0.28% and an axial force resultant of 237 MPa mm.

Beyond this threshold, the curve becomes nonlinear, with increased energy dissipation and a corresponding decrease in effective modulus, reflecting the accumulation of damage. The ultimate force resultant occurs at a maximum load of 435 MPa mm and a strain of 0.55%. Energy dissipation increases sharply as the resultant force reaches its peak.

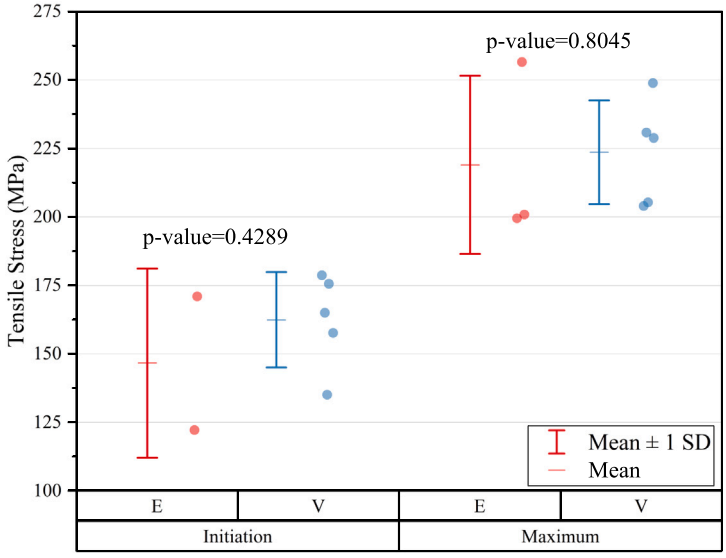


**Fig. 6.** Variability of damage initiation and maximum tensile strength in experimental (E) and virtual (V) specimens.

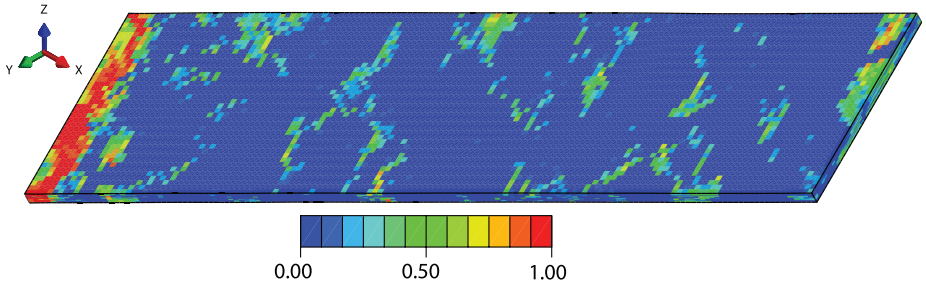


**Fig. 7.** Spatial distribution of matrix failure $d_m$ in tension at a nominal strain of $\hat{\varepsilon}_{11} = 0.58\%$ for a fully-discontinuous specimen.

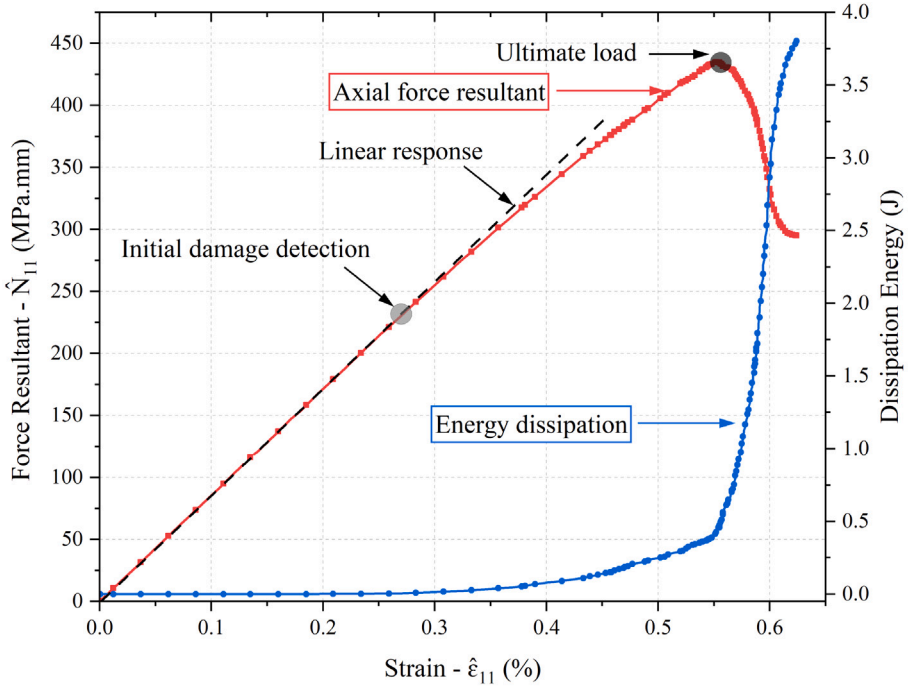


**Fig. 8.** Effective force resultant $\hat{N}_{11}$ and dissipation energy as a function of the axial strain $\hat{\varepsilon}_{11}$ for a fully-random short tape (discontinuous) thermoplastic composite specimen under tensile load.

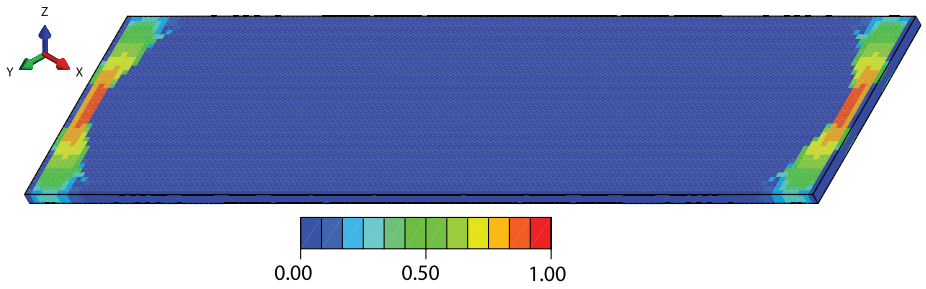


**Fig. 9.** Spatial distribution of fiber damage $d_f$ in tension at a nominal strain of $\hat{\epsilon}_{11} = 1.63\%$ for a fully-continuous specimen.

The quasi-static simulation is only able to capture part of the post-peak response. The curve shown in 8 is terminated at the latest converged state, but the numerical simulation is unable to determine the full extent of the fracture energy of the material. Nevertheless, the simulation is able to establish two representative values, namely the onset of detectable damage at 0.28% and the ultimate load at a strain of 0.55%. This considerable strain range between initial detection and peak load reflects the material's ability to undergo significant deformation before reaching its ultimate strength, showcasing its resilience and capacity for pseudoductility under tensile loading conditions (damage tolerance).

#### 4.1.2. Fully continuous specimen

The second type of specimens analyzed are made only out of continuous tapes in the longitudinal direction (i.e., all $N = 20$ plies are made out of 0° UD tapes aligned in the longitudinal direction of the specimen). As in the previous case, this configuration is also expected to be a limit case but now in terms of higher values for elastic stiffness and fracture strength.

The specimen is loaded until failure, which in this case is dominated by fiber failure in tension. Fig. 9 depicts the spatial distribution of the fiber damage $d_f$ in tension at a nominal axial strain $\hat{\epsilon}_{11} = 1.63\%$, which corresponds to a point slightly after the ultimate strength. As shown in the figure, the fiber damage localizes close to the end tabs due to a slight concentration of stresses, but otherwise failure could have localized elsewhere in the presence of imperfections. However, it is worth pointing out that the specimen still has a non-negligible residual strength at the state shown in the figure since the damage needs to further localize and fully break a cross-section of the specimen.

The effective axial force resultant $\hat{N}_{11}$ for this configuration is plotted as a function of the effective axial strain $\hat{\epsilon}_{11}$ in Fig. 10. As can be observed in the figure, the response is approximately linear until the point of initial (detectable) damage at an axial strain of 1.5716% and an axial force resultant of 4023 MPa mm. Soon after the initial detection of damage, the peak axial force resultant of 4027 MPa mm is reached at a strain of 1.5736%. Only one small portion of the post-peak response is shown as the simulation was not able to converge beyond that point. Correspondingly, the information about the fracture energy of this configuration is somewhat limited. Nevertheless, the relatively small strain span from detection of damage to peak load is an indication of a brittle response, which is to be expected for this configuration since it is dominated by fiber fracture in all plies.

#### 4.1.3. Specimens with 50% hybridization ratio

To illustrate the mechanical performance of hybrid continuous–discontinuous tape composites, the effective axial force resultant $\hat{N}_{11}$ as a function of the effective axial strain $\hat{\epsilon}_{11}$ are reported in Fig. 11 for samples with the same hybridization ratio of 50% but distinct spatial distribution, namely the inward-to-outward, intercalated and outward-to-inward hybrid configurations. For comparison purposes, the mechanical responses of the fully continuous and fully random cases, shown respectively in Figs. 8 and 10, are reproduced in Fig. 11.

The samples with the same hybridization ratio of 50% show a similar mechanical response, which was anticipated since the spatial distribution should not have a major influence for the case of tensile loading (Fig. 11). The effective elastic stiffness in all three hybrid configurations is similar, and the peak loads are also comparable, partially validating the numerical simulations. The response of the hybrid continuous–discontinuous tape composites is bounded by the fully random (discontinuous) and fully continuous tape cases in terms of stiffness and ultimate load. Fig. 11 omits energy dissipation but shows that the response for the 50% hybridization ratio is qualitatively bounded between the fully discontinuous and fully continuous configurations.

### 4.2. Bending behavior of distinct configurations

#### 4.2.1. Fully discontinuous specimen

Similar to the tension case, the first specimen analyzed is a sample made only of randomly-oriented discontinuous tapes (i.e., 0% hybridization ratio), which is expected to have the lowest properties in terms of stiffness and strength. The sample is loaded under three-point bending conditions until failure, with the top layers in compression and the bottom layers in tension. Failure is expected to initiate in the matrix where the fibers are misaligned with the load. Correspondingly, Fig. 12 shows the damage variable for matrix failure: (a) compression failure in the top layer and (b) tension failure in the bottom layer. Note that Fig. 12(b) is a rotated view of the bottom of the specimen for clarity.

As seen in the figure, matrix failure under tension in (b) is more pronounced than compression failure in (a), highlighting that the weakest aspect of this configuration is the misaligned layers subjected to tensile loads. The top section provides damage tolerance after the bottom layers fail.

The effective moment resultant $\hat{M}_{11}$ for the specimen is shown in Fig. 13 as a function of the effective curvature $\hat{\kappa}_{11}$. The figure also includes the energy dissipated as a function of the curvature. The response of the specimen is mostly linear prior to the initial detection of damage based on the criterion outlined in Section 2.5, which occurs at an effective curvature of $\hat{\kappa}_{11} = 0.0042\ \text{mm}^{-1}$ and at an effective moment resultant $\hat{M}_{11} = 124\ \text{MPa mm}^2$. Subsequently, under increased loading, the effective bending moment reaches its ultimate value of $\hat{M}_{11} = 138\ \text{MPa mm}^2$ at an effective curvature of $\hat{\kappa}_{11} = 0.0048\ \text{mm}^{-1}$.

The curve is terminated at the last converged state, which occurs shortly after reaching the ultimate bending moment resultant. As opposed to the case of tensile loading analyzed in Section 4.1.1, the range from the initial detection of damage to the ultimate loading shown in Fig. 13 is relatively narrow, which indicates a more brittle behavior under bending than under axial tension.

#### 4.2.2. Fully continuous specimen

The next sample analyzed is made only of continuous tapes with fibers oriented in the axial direction and loaded under three-point bending conditions until failure. This sample is expected to have the highest stiffness and fracture strength under bending, with the top layers under compression and the bottom layers under tension.

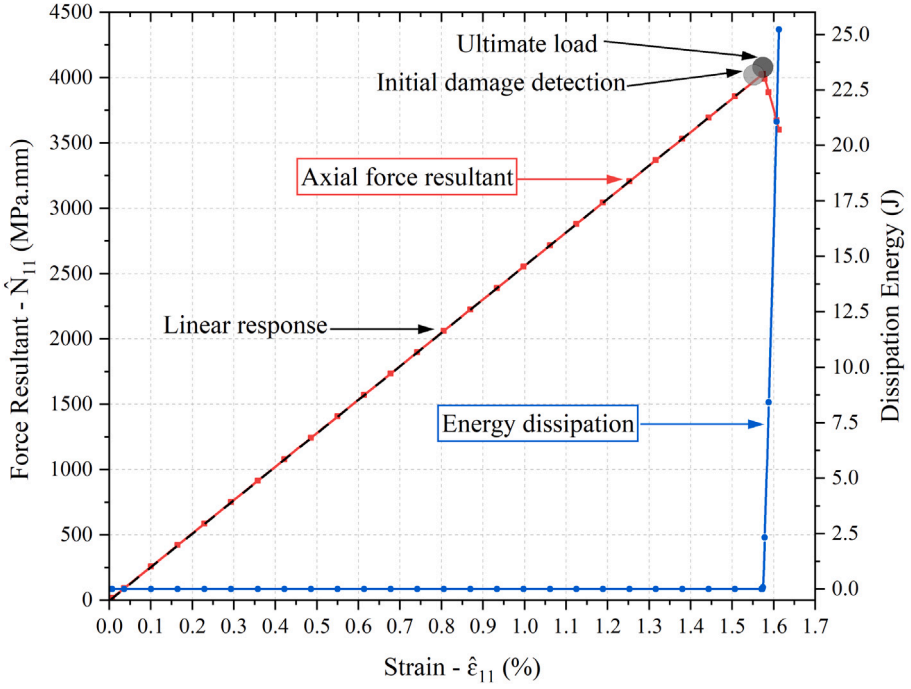


**Fig. 10.** Effective force resultant $\hat{N}_{11}$ and dissipation energy as a function of the axial strain $\hat{\epsilon}_{11}$ for a continuous thermoplastic composite specimen under tensile load.

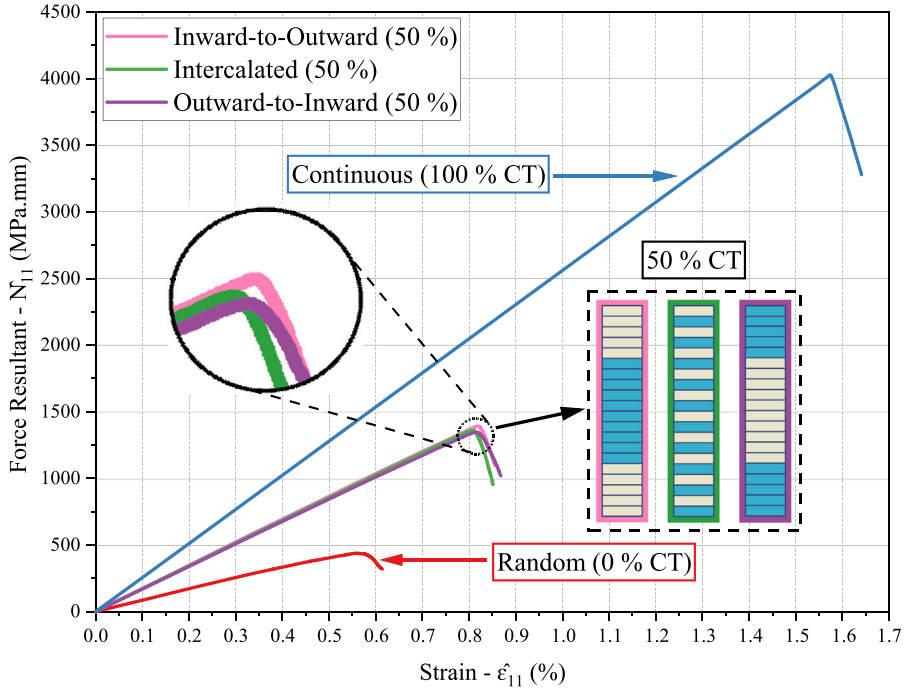


**Fig. 11.** Effective force resultant $\hat{N}_{11}$ as a function of the axial strain $\hat{\epsilon}_{11}$ for various hybrid continuous–discontinuous tape thermoplastic composite specimen with 50% hybridization ratio of 50% under tensile load. The limit cases of fully-continuous (100% ratio) and fully-discontinuous (0% ratio) are reproduced here for ease of comparison.

The effective bending moment resultant $\hat{M}_{11}$ and the energy dissipated for this specimen is shown in Fig. 14 as a function of the resultant curvature $\hat{\kappa}_{11}$. As can be observed in the figure, the initial detection of damage and the ultimate load point are close to each other, which confirms the brittle nature of the specimen made only out of continuous tapes. The numerical simulation indicates the presence of an ultimate value, but otherwise is unable to proceed beyond the peak value, hence the value of the effective fracture energy cannot be established accurately.

#### 4.2.3. *Specimens with 50% hybridization ratio*

The third case analyzes hybrid samples under three-point bending. Depending on the spatial configuration, failure occurs due to matrix or fiber failure, or a combination of both. To assess the performance of hybrid samples with a 50% hybridization ratio, three configurations—outward-to-inward, intercalated, and inward-to-outward—are analyzed. These configurations are expected to perform as best, intermediate, and worst, respectively, and the analysis aims to quantify these expectations.

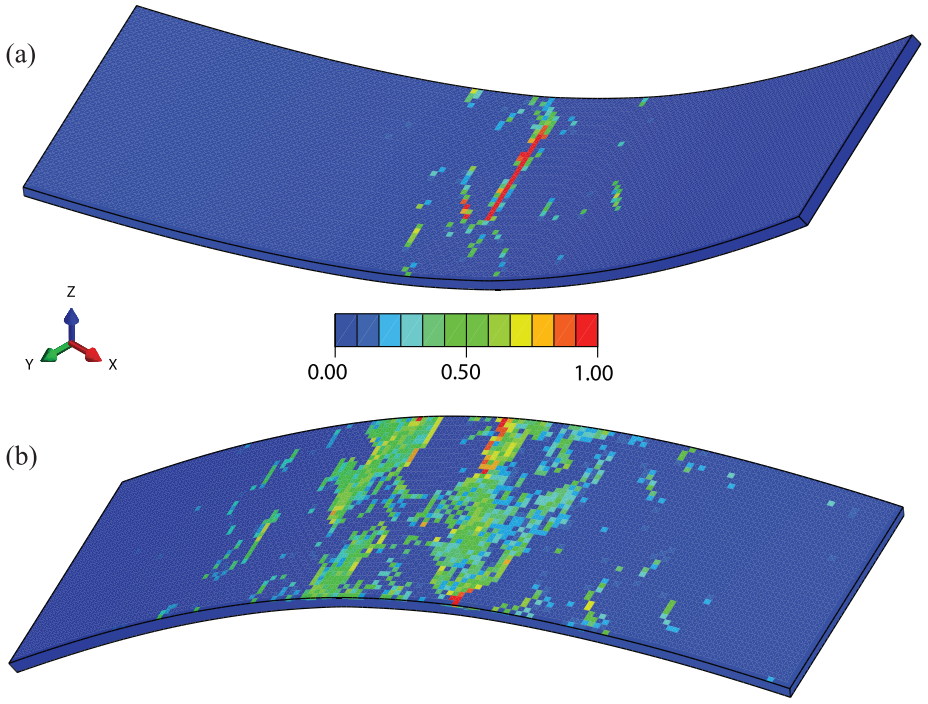


**Fig. 12.** Damage variable $d_m$ in (a) matrix compression for the top layer and in (b) matrix tension for the bottom layer of a specimen made only of randomly-distributed discontinuous tapes loaded under three point bending up to an effective curvature $\hat{\kappa}_{11} = 0.0048$ mm$^{-1}$. Both (a) and (b) correspond to the same specimen, with (a) being the top view and (b) a rotated view of the bottom of the specimen.

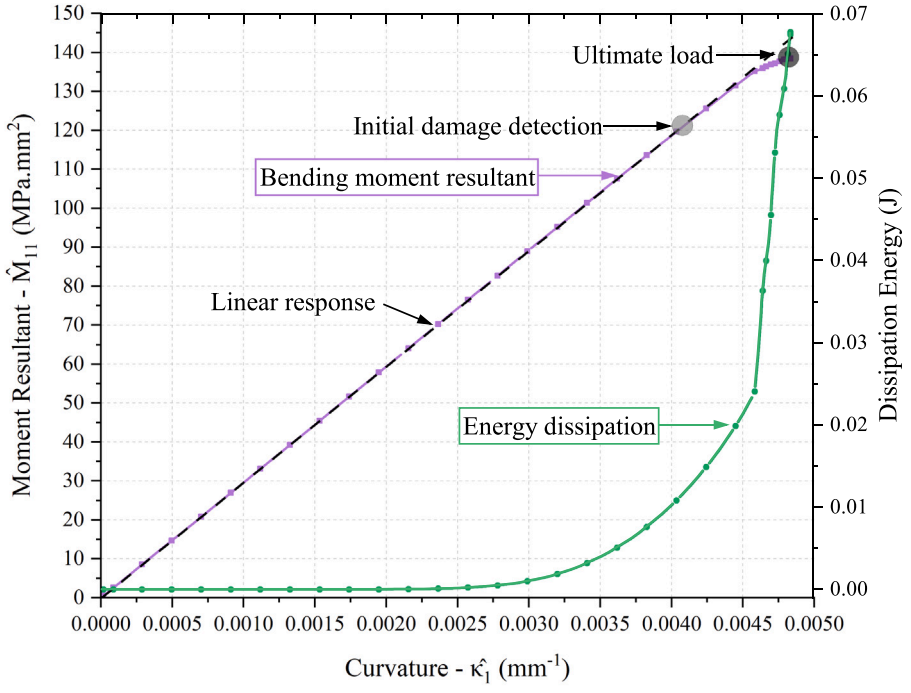


**Fig. 13.** Effective moment resultant $\hat{M}_{11}$ and dissipation of energy as functions of the effective curvature $\hat{\kappa}_{11}$ for a specimen made of discontinuous tapes only under three point bending load.

In Fig. 15, the bending response of hybrid continuous–discontinuous thermoplastic composite specimens featuring 50% hybridization ratio are shown, where the effective bending moment resultant $\hat{M}_{11}$ is plotted as a function of the effective curvature $\hat{\kappa}_{11}$. The response curves for the fully-continuous (100% hybridization) and fully-discontinuous (0% hybridization) specimens are shown for comparison. For the 50% hybridization ratio, three configurations, namely inward-to-outward, finely intercalated, and outward-to-inward, are analyzed. Unlike tensile loading, the configuration's impact on bending behavior is more pronounced, even with the same hybridization ratio.

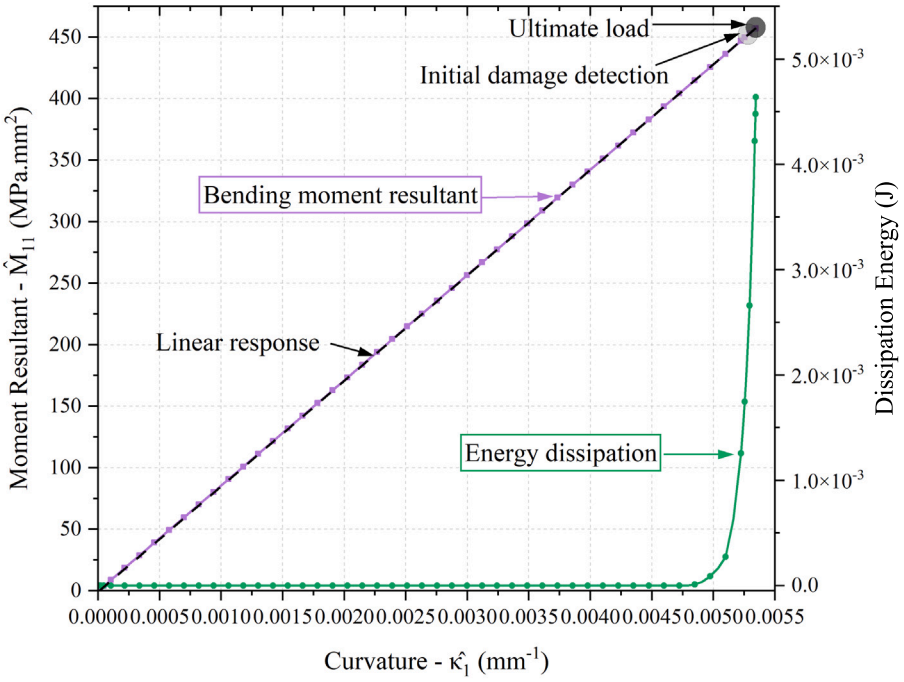


**Fig. 14.** Effective moment resultant $\hat{M}_{11}$ and dissipation of energy as functions of the effective curvature $\hat{\kappa}_{11}$ for a specimen made of continuous tapes only under three point bending load.

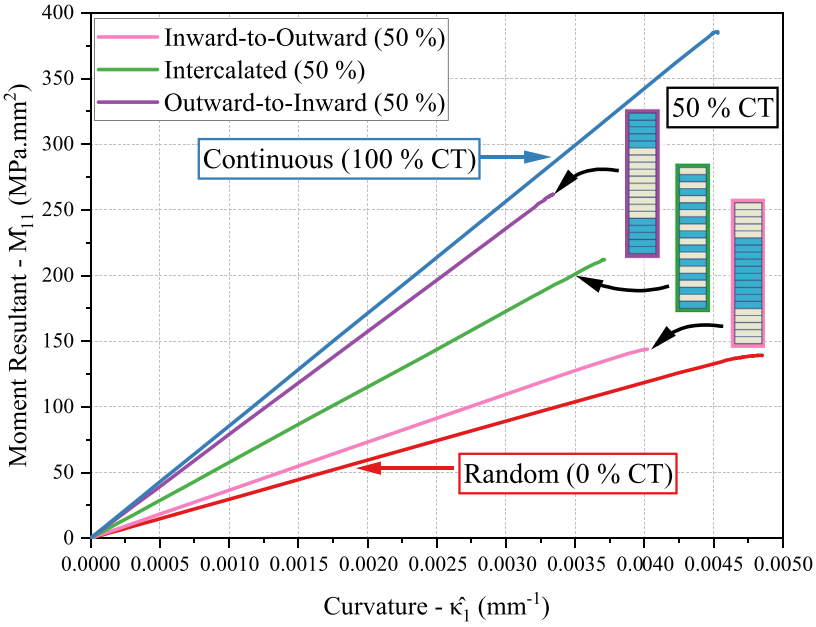


**Fig. 15.** Effective bending moment resultant $\hat{M}_{11}$ as a function of the effective curvature $\hat{\kappa}_{11}$ for various hybrid continuous–discontinuous tape thermoplastic composite specimen with 50% hybridization ratio of 50% under three-point bending. The limit cases of fully-continuous (100% ratio) and fully-discontinuous (0% ratio) are reproduced here for ease of comparison.

The bending stiffness of the 50% outward-to-inward specimen closely matches that of the fully-continuous specimen, highlighting the influence of the outer layers. Its ultimate strength is about 30% lower than the fully-continuous specimen, indicating good performance. Failure initiates in the inner layers. The 50% inward-to-outward specimen has similar stiffness to the fully-random specimen, with strength comparable to the fully-discontinuous specimen, both dominated by matrix failure in the outer layers. The finely intercalated specimen shows intermediate stiffness and strength. In general, the outward-to-inward configuration outperforms the inward-to-outward configuration in terms of stiffness and strength. This is essentially due to the fact that the stresses under bending are higher in the outmost layers. Since the outward-to-inward configurations have continuous tapes in the outer layers, then the overall performance is better compared to the inward-to-outward configuration that places the weakest material (discontinuous tapes) in the critical outer layers.

## 5. Effect of configurations and hybridization ratio on elastic properties

A key goal of hybrid materials is to combine the properties of continuous and discontinuous tapes. Continuous tapes aim to enhance overall

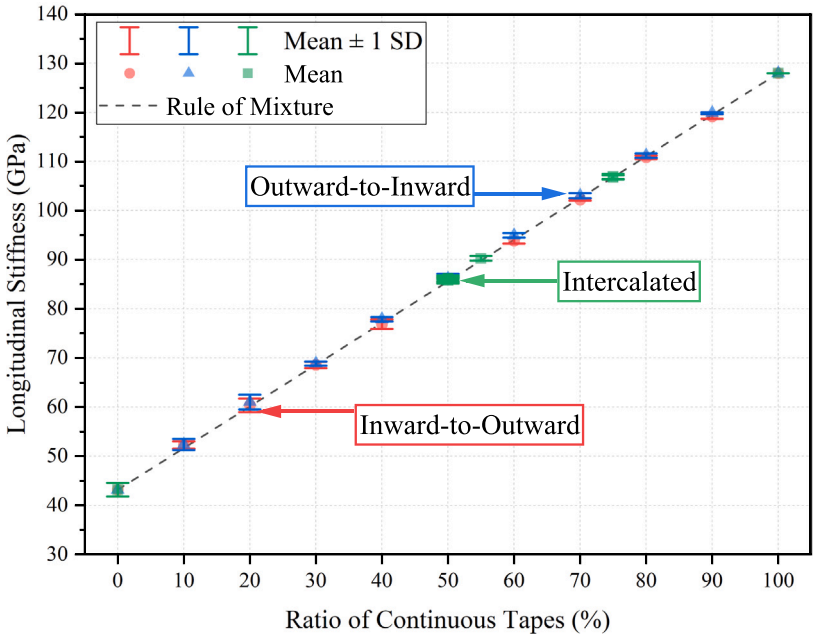


**Fig. 16.** Comparison of effective longitudinal stiffness under uniaxial tension for inward-to-outward, outward-to-inward and intercalated configurations.

stiffness, ideally proportional to their volume content (hybridization ratio). This section analyzes the effective elastic stiffness under tension and bending for different configurations and hybridization ratios.

### 5.1. Elastic properties under tensile loading

Fig. 16 shows the tensile longitudinal stiffness as a function of hybridization ratio for various configurations: inward-to-outward (red), outward-to-inward (blue), and intercalated (green). For configurations with randomly-oriented discontinuous tapes, six random realizations are used to capture fluctuations, with the mean and standard deviation shown. No significant differences in longitudinal stiffness are observed among the configurations, and the simulations confirm that a simple rule of mixtures can estimate the hybrid material's stiffness, within the fluctuations.

### 5.2. Elastic properties under bending loading

The bending stiffness under three-point bending as a function of hybridization ratio, revealing significant differences between the inward-to-outward and outward-to-inward configurations, as illustrated in Fig. 17. For configurations with randomly-oriented discontinuous tapes, six realizations were used to calculate the mean and standard deviation.

As shown in Fig. 17, the outward-to-inward configuration quickly increases bending stiffness with a small addition of continuous tapes, but this effect saturates at higher hybridization ratios. In contrast, the inward-to-outward configuration shows a gradual stiffness increase initially, which accelerates as the hybridization ratio approaches 100%. The inward-to-outward configuration also exhibits greater variability between random realizations, especially at low hybridization ratios, due to the influence of randomly oriented outer layers during bending.

For intercalated configurations with 25%, 50%, and 75% hybridization ratios, the bending stiffness generally follows a rule of mixtures. Nevertheless, deviations occur when both the top and bottom layers consist of continuous tapes. The stiffness of a 55% hybridization sample (S3C6 in Fig. 1) is notably higher than that of 50% samples (S3C1–S3C5), where at least one external layer contains discontinuous tapes. This highlights the significant influence of continuous tapes in the outer layers.

## 6. Effect of configurations and hybridization ratio on the initial and ultimate failure strengths

The strength was characterized by two points: (i) initial failure strength (load at first damage detection) and (ii) ultimate failure strength (maximum load). To assess damage tolerance, the energy dissipated between initial failure and ultimate strength is used as an indicator of toughness.

Fig. 18 presents the initial and ultimate strengths for intercalated configurations under bending, measured as critical bending moment resultants, for various hybridization ratios and intercalation arrangements (fine and coarse). For comparison, values for the 0% (purely discontinuous tapes) and 100% (purely continuous tapes) hybridization cases are included. The energy dissipated up to ultimate strength is also shown, using the scale on the right. The specific intercalated configurations S3C*n* are detailed in Fig. 1.

In terms of initial strength, Fig. 18 shows that for intercalated configurations with a 50% hybridization ratio, sample S3C4 has lower initial strength than other samples (S3C1–S3C5) due to more discontinuous tapes in the bottom layers, which fail earlier under tensile load. This premature failure also results in higher energy dissipation. Despite of this, the ultimate strength for all 50% samples remains similar within the fluctuations of random realizations. A similar trend is observed for the 75% hybridization ratio, where S3C8 has lower initial strength than S3C7 due to bottom-layer discontinuous tapes in tension versus top-layer tapes in compression. Nonetheless, the ultimate strength of samples S3C7 and S3C8 are similar. Hence, while initial strength varies, ultimate strength under bending is less sensitive to intercalation details.

Regarding the increase in ultimate strength in bending with the addition of continuous tapes, the values for 0%, 25%, 50% and 75% show a steady strengthening, but jumps significantly at 100%. In contrast, energy dissipation decreases rapidly as the continuous tape content increases. These results are consistent with the role of the continuous and discontinuous tapes, namely that the continuous tapes are efficient at carrying mechanical loads (uninterrupted) while discontinuous tapes enhance pseudoductility.

## 7. Conclusions and recommendations

A systematic investigation of various configurations and stacking sequences reveals key factors influencing the stiffness, strength, and

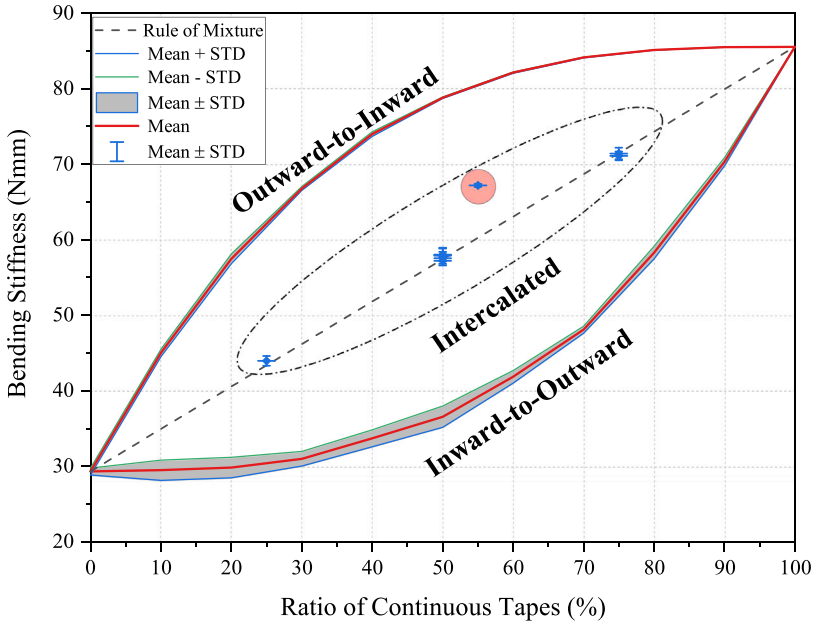


**Fig. 17.** Comparison of effective bending stiffness under three point bending for inward-to-outward, outward-to-inward and intercalated configurations. The stiffness for the intercalated configuration with a 55% hybridization ratio (corresponding to the configuration labeled as S3C6 in Fig. 1) is highlighted in red.

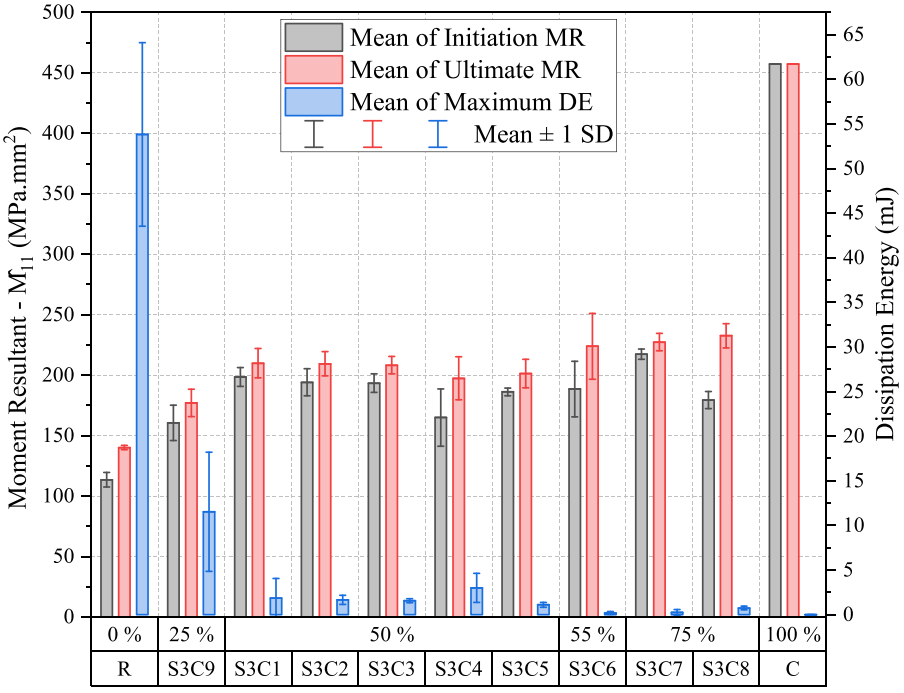


**Fig. 18.** Initial and ultimate strength (measured in terms of bending moment resultants (MR) for a laminate) and dissipation of energy (DE) for various intercalation arrangements and hybridization ratios under bending loading. The limit cases of a laminate made out of purely discontinuous tapes (R) and purely continuous tapes (C) are included for reference.

damage tolerance of hybrid laminates made from continuous and discontinuous tapes. For stiffness, the ratio of continuous tapes is critical, showing a linear correlation under tensile loading for all stacking sequences. Under bending, placing continuous tapes on the outer layers, similar to an I-beam design, greatly improves stiffness, while the opposite arrangement yields sub-optimal performance. The intercalated approach also shows a near-linear stiffness correlation, though it can depend on whether the outer layers are occupied by continuous tapes.

The ultimate strength of the laminate under tensile load correlates approximately linearly with the ratio of continuous tapes except for values close to 100%, where a significant increase occurs. The damage tolerance in tension, as measured indirectly by energy dissipation, showing a brittle-like behavior. This behavior is observed for all stacking sequences analyzed in tension. Under bending, placing discontinuous tapes on the outer layers provides good damage tolerance but has a sub-optimal performance in terms of strength. Conversely, placing continuous tapes on the outer layers results in enhanced strength, but at the expense of damage tolerance. Intercalated arrangements tend to provide enhanced strength but limited damage tolerance.

The present study indicates that the strategy to add layers of continuous tapes to a laminate made out of discontinuous tapes to enhance strength and stiffness or, conversely, the strategy to add layers of

discontinuous tapes to a laminate made out of continuous tapes to enhance damage tolerance, requires a detailed analysis of the expected loading conditions to optimize the trade-off between these properties. Under uniaxial tension, the main factor is the hybridization ratio, while the stacking sequence plays a secondary role. For bending loading, both the hybridization ratio and the details of the stacking sequence are important, where an optimization strategy would depend on a required performance trade-off for the hybrid material.

It is important to point out that the conclusions of the present study on damage tolerance are limited by the fact that the fracture energy of the specimens could not be established since the simulations did not converge until final failure. A different modeling strategy is required to determine the actual fracture energy and, thus, to quantify damage tolerance more accurately.

## CRediT authorship contribution statement

**Deniz Ezgi Gulmez:** Writing – original draft, Visualization, Software, Methodology, Investigation, Formal analysis, Conceptualization. **Sergio Turteltaub:** Writing – original draft, Methodology, Conceptualization.

## Declaration of competing interest

The authors declare the following financial interests/personal relationships which may be considered as potential competing interests: This work was supported by the Fraunhofer-Gesellschaft. The funder played no role in the study design, data collection and analysis, decision to publish, or preparation of the manuscript. The authors have no other conflicts of interest to declare.

## Acknowledgments

We would like to thank Fraunhofer-Gesellschaft, Germany for their financial support. The authors also appreciate Professor Clemens Dransfeld from TU Delft for providing access to materials and manufacturing facilities used for experimental validation.

## Data availability

Data will be made available on request.

## References

[1] Pimenta S, Pinho ST. Recycling carbon fibre reinforced polymers for structural applications: Technology review and market outlook. Waste Manage 2011;31(2):378–92.
[2] Timmis AJ, Hodzic A, Koh L, Bonner M, Soutis C, Schäfer AW, Dray L. Environmental impact assessment of aviation emission reduction through the implementation of composite materials. Int J Life Cycle Assess 2015;20(2):233–43.
[3] Lefeuvre A, Garnier S, Jacquemin L, Pillain B, Sonnemann G. Anticipating in-use stocks of carbon fiber reinforced polymers and related waste flows generated by the commercial aeronautical sector until 2050. Resour Conserv Recycl 2017;125(June):264–72.
[4] Stelzer PS, Cakmak U, Eisner L, Doppelbauer LK, Kállai I, Schweizer G, Prammer HK, Major Z. Experimental feasibility and environmental impacts of compression molded discontinuous carbon fiber composites with opportunities for circular economy. Compos Part B: Eng 2022;234(July 2021).
[5] Hagnell MK, Åkermo M. The economic and mechanical potential of closed loop material usage and recycling of fibre-reinforced composite materials. J Clean Prod 2019;223:957–68.
[6] Zhang J, Chevali VS, Wang H, Wang CH. Current status of carbon fibre and carbon fibre composites recycling. Compos Part B: Eng 2020;193(April):108053.
[7] Yu H, Potter KD, Wisnom MR. A novel manufacturing method for aligned discontinuous fibre composites ( high performance-discontinuous fibre method ). Compos Part A: Appl Sci Manuf 2014;65:175–85.
[8] Henry J, Pimenta S. Semi-analytical simulation of aligned discontinuous composites. Compos Sci Technol 2017;144:230–44.
[9] Pimenta S, Robinson P. An analytical shear-lag model for composites with 'brick-and-mortar' architecture considering non-linear matrix response and failure. Compos Sci Technol 2014;104:111–24.
[10] Czél G, Pimenta S, Wisnom MR, Robinson P. Demonstration of pseudo-ductility in unidirectional discontinuous carbon fibre/epoxy prepreg composites. Compos Sci Technol 2015;106:110–9.
[11] Johanson K, Harper LT, Johnson MS, Warrior NA. Heterogeneity of discontinuous carbon fibre composites: Damage initiation captured by digital image correlation. Compos Part A: Appl Sci Manuf 2015;68:304–12.
[12] Fuller JD, Wisnom MR. Pseudo-ductility and damage suppression in thin ply CFRP angle-ply laminates. Compos Part A: Appl Sci Manuf 2015;69:64–71.
[13] Fuller JD, Wisnom MR. Exploration of the potential for pseudo-ductility in thin ply cfrp angle-ply laminates via an analytical method. Compos Sci Technol 2015;112:8–15.
[14] Yu HN, Longana ML, Jalalvand M, Wisnom MR, Potter KD. Hierarchical pseudo-ductile hybrid composites combining continuous and highly aligned discontinuous fibres. Compos Part A: Appl Sci Manuf 2018;105:40–56.
[15] Czél G, Jalalvand M, Wisnom MR. Design and characterisation of advanced pseudo-ductile unidirectional thin-ply carbon/epoxy-glass/epoxy hybrid composites. Compos Struct 2016;143:362–70.
[16] Longana ML, Yu HN, Jalavand M, Wisnom MR, Potter KD. Aligned discontinuous intermingled reclaimed/virgin carbon fibre composites for high performance and pseudo-ductile behaviour in interlaminated carbon-glass hybrids. Compos Sci Technol 2017;143:13–21.
[17] Alves M, Pimenta S. The influence of 3D microstructural features on the elastic behaviour of tow-based discontinuous composites. Compos Struct 2020;251(September 2019):112484.
[18] Chen Z, Huang T, Shao Y, Li Y, Xu H, Avery K, Zeng D, Chen W, Su X. Multiscale finite element modeling of sheet molding compound (SMC) composite structure based on stochastic mesostructure reconstruction. Compos Struct 2018;188(September 2017):25–38.
[19] Selezneva M, Lessard L. Characterization of mechanical properties of randomly oriented strand thermoplastic composites. J Compos Mater 2016;50(20):2833–51.
[20] Kravchenko SG, Sommer DE, Denos BR, Favaloro AJ, Tow CM, Avery WB, Pipes RB. Tensile properties of a stochastic prepreg platelet molded composite. Compos Part A: Appl Sci Manuf 2019;124(July):105507.
[21] Alves M, Li Y, Pimenta S. Spatial variability and characteristic length-scales of strain fields in tow-based discontinuous composites: Characterisation and modelling. Compos Part B: Eng 2023;262(May):110789.
[22] Selezneva M, Roy S, Lessard L, Yousefpour A. Analytical model for prediction of strength and fracture paths characteristic to randomly oriented strand (ROS) composites. Compos Part B: Eng 2016;96:103–11.
[23] Bernatas R, Dagreou S, Despax-Ferreres A, Barasinski A. Recycling of fiber reinforced composites with a focus on thermoplastic composites. Clean Eng Technol 2021;5:100272.
[24] Trauth A, Weidenmann KA. Continuous-discontinuous sheet moulding compounds – effect of hybridisation on mechanical material properties. Compos Struct 2018;202(May):1087–98.
[25] Trauth A, Weidenmann KA, Altenhof W. Puncture properties of a hybrid continuous-discontinuous sheet moulding compound for structural applications. Compos Part B: Eng 2019;158(May 2018):46–54.
[26] Hasan MMB, Abdkader A, Cherif C, Spennato F. Fibre hybrid composites consisting of discontinuous waste carbon fi bre and continuous glass fi laments developed for load-bearing structures with improved impact strength. Compos Part A 2019;126(May):105610.
[27] Swolfs Y, Gorbatikh L, Verpoest I. Fibre hybridisation in polymer composites: A review. Compos Part A: Appl Sci Manuf 2014;67:181–200.
[28] Swolfs Y, Verpoest I, Gorbatikh L. Recent advances in fibre-hybrid composites: materials selection, opportunities and applications. Int Mater Rev 2019;64(4):181–215.
[29] Visweswaraiah SB, Lessard L, Hubert P. Interlaminar shear behaviour of hybrid fibre architectures of randomly oriented strands combined with laminate groups. Compos Struct 2017;176:823–32.
[30] Visweswaraiah SB, Lessard L, Hubert P. Tensile behaviour of hybrid fibre architectures of randomly oriented strands combined with laminate groups. J Compos Mater 2019;53(26-27):3725–40.
[31] Nakashima Y, Yamashita S, Zhang X, Suganuma H, Takahashi J. Analytical modelling of the behaviour and scatter of the flexural modulus of randomly oriented carbon fibre strand thermoplastic composites. Compos Struct 2017;178:217–24.
[32] Tang H, Zhou G, Sun Q, Avinesh O, Meng Z, Engler-Pinto C, Su X. Experimental and computational analysis of bending fatigue failure in chopped carbon fiber chip reinforced composites. Compos Struct 2021;275.
[33] Qu P, Wan Y, Fang G, Guo A, Liu G, Takahashi J. A novel heterogeneous-particle model based on peridynamics for flexural mechanical properties of randomly oriented fiber reinforced composites. Compos Part B: Eng 2022;243.
[34] Zhang Y, Yang X, Wang X, Zhuang X. A micropolar peridynamic model with non-uniform horizon for static damage of solids considering different nonlocal enhancements. Theor Appl Fract Mech 2021;113.

[35] Gulmez DE, Madonado J, Masania K, Sinke J, Dransfeld C. Quantification of structural response and edge orientation of chopped tape thermoplastic composites in net-shaped specimens. Compos Struct 2023;321(February):117302.
[36] Pappas G, Canal LP, Botsis J. Characterization of intralaminar mode I fracture of AS4/PPS composite using inverse identification and micromechanics. Compos Part A: Appl Sci Manuf 2016;91:117–26.
[37] Hashin Z. Failure criteria for unidirectional fiber composites. J Appl Mech Trans ASME 1980;47(2):329–34.
[38] Lapczyk I, Hurtado JA. Progressive damage modeling in fiber-reinforced materials. Compos Part A: Appl Sci Manuf 2007;38(11):2333–41.